energies

MDPI

Article

Small-Signal Stability Analysis of Photovoltaic-Hydro Integrated Systems on Ultra-Low Frequency Oscillation

Sijia Wang [1], Xiangyu Wu [1,*], Gang Chen [2] and Yin Xu [1]

[1] School of Electrical Engineering, Beijing Jiaotong University, Beijing 100044, China; wangsijia@bjtu.edu.cn (S.W.); xuyin@bjtu.edu.cn (Y.X.)

[2] State Grid Sichuan Electric Power Research Institute, Chengdu 610072, China; gangchen_thu@163.com

* Correspondence: wuxiangyu@bjtu.edu.cn

Received: 24 January 2020; Accepted: 21 February 2020; Published: 24 February 2020



Abstract: In recent years, ultralow-frequency oscillation has repeatedly occurred in asynchronously connected regional power systems and brought serious threats to the operation of power grids. This phenomenon is mainly caused by hydropower units because of the water hammer effect of turbines and the inappropriate Proportional-Integral-Derivative (PID) parameters of governors. In practice, hydropower and solar power are often combined to form an integrated photovoltaic (PV)-hydro system to realize complementary renewable power generation. This paper studies ultralow-frequency oscillations in integrated PV-hydro systems and analyzes the impacts of PV generation on ultralow-frequency oscillation modes. Firstly, the negative damping problem of hydro turbines and governors in the ultralow-frequency band was analyzed through the damping torque analysis. Subsequently, in order to analyze the impact of PV generation, a small-signal dynamic model of the integrated PV-hydro system was established, considering a detailed dynamic model of PV generation. Based on the small-signal dynamic model, a two-zone and four-machine system and an actual integrated PV-hydro system were selected to analyze the influence of PV generation on ultralow-frequency oscillation modes under different scenarios of PV output powers and locations. The analysis results showed that PV dynamics do not participate in ultralow-frequency oscillation modes and the changes of PV generation to power flows do not cause obvious changes in ultralow-frequency oscillation mode. Ultra-low frequency oscillations are mainly affected by sources participating in the frequency adjustment of systems.

Keywords: photovoltaic generation; ultralow-frequency oscillation; small-signal model; eigenvalue analysis; damping torque

1. Introduction

There are differences in mechanism and characteristics between ultralow-frequency oscillation and traditional low-frequency oscillation. The frequency range of low-frequency oscillation is 0.1–2.5 Hz, and frequencies of ultralow-frequency oscillation is below 0.1 Hz. At present, researchers in this field generally believe that ultralow-frequency oscillation is caused by hydropower units. In recent years, ultralow-frequency oscillation has occurred frequently. As early as 1964, a frequency oscillation with a period of about 20 s was observed in the Southwestern United States [1]. Ultralow-frequency oscillations with frequencies below 0.05 Hz have also been observed in Turkey and Bulgaria [2], but due to their small impacts, they have not attracted widespread attention from researchers. In 2016, in an asynchronous networking test conducted by Yunnan Power Grid in China, a relatively severe ultralow-frequency oscillation event occurred, which lasted about half an hour [3]. After tripping the governor of some hydropower units, the oscillation decayed. According to researchers' studies, similar possible troubles of ultralow-frequency oscillations exist in Sichuan Power Grid in China, which also

contains a large number of hydropower units. This problem can be triggered after asynchronous networking [4].

Some researchers have carried out research work on ultralow-frequency oscillation. Ultralow-frequency oscillation is related to governors and turbines. The time constant of the water hammer effect and the governor parameters can change the oscillation frequency and damping [5]. When the proportion of hydropower units in a system is high, ultralow-frequency oscillation is likely to occur. Adjusting the PID parameters of governors or increasing the proportion of thermal power units can suppress this oscillation [6]. Reference [7] did the damping torque analysis and pointed out that ultralow-frequency oscillation was caused by negative damping generated by a regulating system. The improper design of governor parameters caused the negative damping torque to be very large, which affected the damping characteristics of the unit. Reference [8] used the vector margin method to analyze multimachine systems, and the results showed that thermal power units and hydropower units with small time constants of the water hammer effect can increase the vector margin of the system while hydropower units with large time constants of the water hammer effect can reduce the vector margin. Reference [9] built a small-signal model of a hydropower system and analyzed the change of the damping of the ultralow-frequency oscillation mode when the PID parameters of a governor were changed through a characteristic analysis method. Changing parameters can increase the damping ratio of the system and suppress the ultralow-frequency oscillation of the system.

With the development of distributed generation technology [10], more photovoltaic (PV) generation is connected to hydropower systems to realize an integrated system, which can make electricity complementary. As a renewable energy, solar power plays an increasingly important role in power systems. However, due to the strong correlation between the light intensity received by surface and environmental factors, the PV output power is random [11]. The output power can be maintained in a stable state, when the weather is clear and the sunlight is direct. However, when the weather is cloudy, the output power will decrease sharply in a short time. Such strong fluctuations can have a huge impact on the stability of the power system. Hydropower can quickly adjust its output power to complement the output power of solar power generation, which can realize smooth power generation for the integrated system. The access of PV changes the dynamic characteristics and power flow of the system, which may affect oscillation modes [12]. Reference [13] analyzed the impact of PV stations on a hydropower system from the perspectives of frequency characteristics, voltage characteristics, and stability. The impact of PV access on low-frequency oscillations of hydropower systems has been extensively studied.

Reference [14] pointed out that renewable energy including wind power and solar power could result in new low-frequency oscillation modes. Reference [15] focused on the damping of local-mode power system oscillations and pointed out that, through eigenvalue analysis, the impact of PV power generation on the small-signal stability of power systems can be positive or negative. Reference [16] showed that, as PV penetration increases and PV replace synchronous motors, the inertia and damping torque of a hydropower system decrease, which may reduce system damping. Reference [17] concluded that the influence factors include permeability, network topology, and disturbance patterns. Reference [18] believed that, although PV dynamics do not participate in low-frequency oscillation modes, the access of PV changes the output of the synchronous system of an original system and the power flow distribution of the system, thereby affecting the low-frequency oscillation mode. However, whether PV generations will have similar effects on ultralow-frequency oscillations has not been studied to give certain conclusions.

Motivated by the aforementioned limitations, this paper studied the impact of PV access on the ultralow-frequency oscillation mode of a hydropower system. Considering the dynamics of the PV generation, a detailed small-signal model of an integrated PV-hydro system was built. The small-signal stability analysis method was used to analyze the influence of the PV generation. Based on a two-zone and four-machine system and an actual system, the influences of different output powers and locations of the PV generation on ultralow-frequency oscillation were analyzed and explained.

The rest of this paper is organized as follows. Section 2 analyzes the damping characteristics of governors and turbines. Section 3 builds a detailed small-signal model of an integrated PV-hydro system. Section 4 analyzes the influence of PV generation on ultralow-frequency oscillation. Conclusions derived from these analyses are presented in Section 5.

2. Damping Torque Analysis

Negative damping problems of hydropower units in the ultralow-frequency band are mainly caused by the water hammer effect of a turbine and improper governor parameters. The damping torque analysis of the hydraulic turbine and the governor can obtain the damping characteristics of the ultralow-frequency band. In the following, we provide a damping torque analysis for a single hydropower unit, which reveals the basic mechanism and impact factors of ultralow-frequency oscillations [19].

The open-loop system model of a governor and a turbine is shown in Figure 1.

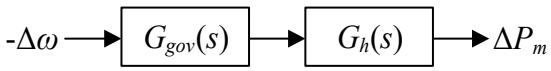


Figure 1. Open-loop system for a governor and a turbine. Symbols: ω, rotating speed; G_{gov}, governor transfer function; G_h, turbine transfer function; P_m, mechanical power.

The turbine transfer function was written as:

$$G_h(s) = \frac{1 - T_W s}{1 + 0.5 T_W s}, \tag{1}$$

where T_w is the water hammer time constant.

The governor transfer function was described as:

$$G_{gov}(s) = \frac{K_D s^2 + K_P s + K_I}{b_p K_I + s} \frac{1}{1 + T_G s}, \tag{2}$$

where K_P, K_I, and K_D are the proportional, integral, and differential parameters, respectively, b_p is the adjustment coefficient, and T_G is the time constant of the servo system.

The open-loop transfer function of the governor and turbine system was expressed as:

$$G_{OpenLoop} = G_{gov} G_h. \tag{3}$$

Decomposing Equation (3) in the $\Delta\delta - \Delta\omega$ coordinate system, Equation (4) can be obtained as:

$$-\Delta P_m = D_T \Delta\omega + S_T \Delta\delta, \tag{4}$$

where D_T is the damping torque and S_T is the synchronous torque. The torque position is shown in Figure 2. For $D_T > 0$, it provides positive damping to the system.

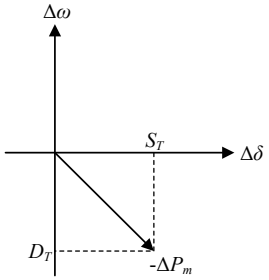
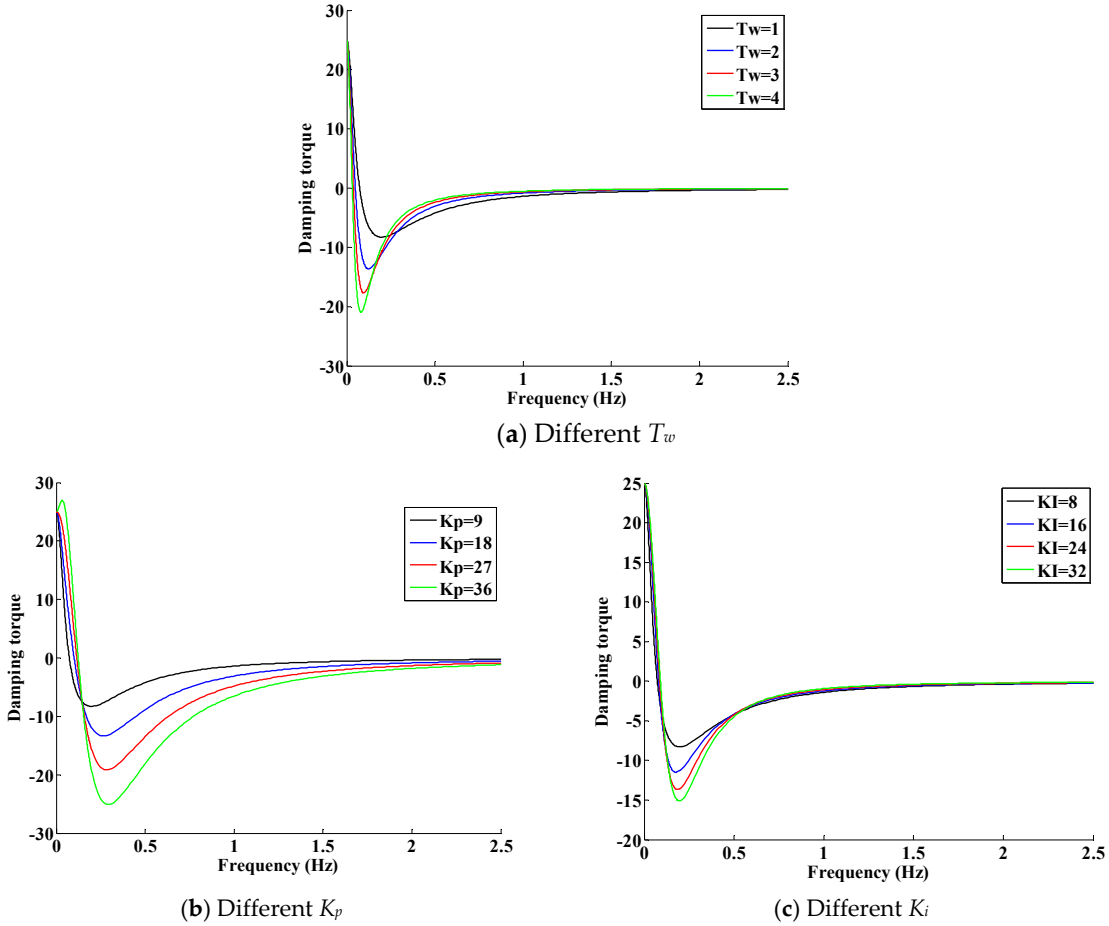


Figure 2. The position of mechanical torque.

The damping characteristics of a system composed of a governor and a turbine in a frequency range of 0–2.5 Hz are shown in Figure 3. For the water hammer time constant T_w, a larger T_w had a more negative damping torque in the ultralow-frequency band. For K_P and K_I in the PID governor, a larger value had more negative damping in the ultralow-frequency band. K_D is generally set to 0. However, the water hammer effect is an inherent characteristic of hydro turbines and cannot be changed. The primary frequency regulation ability of a governor generally requires larger K_P and K_I, which contradicts the suppression of ultralow-frequency oscillation.



(**a**) Different T_w

(**b**) Different K_p

(**c**) Different K_i

Figure 3. The damping characteristics of the governor and the turbine in a frequency range of 0–2.5 Hz.

Although the damped torque analysis method can analyze the damping characteristics of the governor and the turbine at different frequencies, it is difficult to analyze multimachine systems and the impact of PV generation.

3. Small-Signal Dynamic Model of an Integrated PV-Hydro System

In order to analyze the impact of PV generation on the ultra-low-frequency oscillation mode of multimachine systems, a detailed small-signal model of an intergrated PV-hydro system needed to be established for small-signal stability analysis.

3.1. Modeling of PV Generation

A PV generation model mainly included a PV array, an inverter, and controllers. Figure 4 shows the structure of a PV generation model connected to a power system.

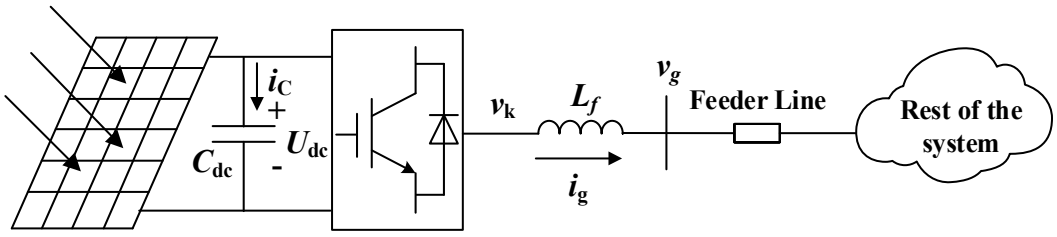


Figure 4. The structure of photovoltaic (PV) generation. Symbols: C_{dc}, direct current (DC) capacitor; U_{dc}, DC-side output voltage; i_C, the current of a DC capacitor; V_k, alternating current (AC)-side output voltage; L_f, AC inductor; i_g, AC-side output current; V_g, the voltage of the point connected with a power system.

3.1.1. PV Array

The accurate model of a PV cell is very complicated, and some parameters are difficult to measure directly [20]. Thus, it is not convenient for research and application. By simplifying calculation equations, a practical engineering model was used in this paper [21]. The standard conditions for PV cells are S_{ref} = 1000 W/m^2 and T_{ref} = 25 °C. In addition, the voltage–current equation under nonstandard conditions can be descried as:

$$I = I_{sc}[1 - C_1(e^{\frac{U}{C_2 U_{oc}}} - 1)], \tag{5}$$

$$C_2 = \frac{U_m/U_{oc} - 1}{\ln(1 - I_m/I_{sc})}, \tag{6}$$

$$C_1 = (1 - I_m/I_{sc})\exp(-U_m/C_2 U_{oc}), \tag{7}$$

where I_{sc} is the short-circuit current, U_{oc} is the open-circuit voltage, I_m and U_m are the current and the voltage at the maximum power, respectively. The parameters under nonstandard conditions can be obtained as:

$$T = T_{air} + kS, \tag{8}$$

$$I_{sc} = I_{scref}(S/S_{ref})[1 + \alpha(T - T_{ref})], \tag{9}$$

$$I_m = I_{mref}(S/S_{ref})[1 + \alpha(T - T_{ref})], \tag{10}$$

$$U_{oc} = U_{ocref}[1 - \gamma(T - T_{ref})]\ln[e + \beta(S/S_{ref} - 1)], \tag{11}$$

$$U_m = U_{mref}[1 - \gamma(T - T_{ref})]\ln[e + \beta(S/S_{ref} - 1)], \tag{12}$$

where T and T_{air} are the temperatures of the PV cell and air, S is the light intensity, U_{ocref} is the open-circuit voltage, I_{scref} is the short-circuit current, U_{mref} is the voltage of the maximum power point, I_{mref} is the current of the maximum power point in standard conditions, and k, α, β, and γ are compensation coefficients.

If the number of PV cells in series is n and the number of parallel connections is m, the voltage and the current of PV array were written as:

$$\begin{cases} U_{dc} = nU \\ I_{dc} = mI \end{cases}. \tag{13}$$

According to Equations (5) and (13), Equation (14) can be obtained as:

$$I_{dc} = mI_{sc}[1 - C_1(e^{\frac{U_{dc}}{nC_2 U_{oc}}} - 1)]. \tag{14}$$

3.1.2. DC Capacitor

Assume that the loss of the inverter can be ignored. Then, the output power of a PV array is equal to the sum of the power of a DC capacitor and the output power of an inverter, which can be described as:

$$U_{dc}I_{dc} = U_{dc}I_C + \frac{3}{2}v_{gd}i_{gd}. \tag{15}$$

The voltage of the capacitor was selected as a state variable, which can be written as:

$$C_{dc}\dot{U}_{dc} = I_C. \tag{16}$$

According to Equations (15) and (16), Equation (17) can be obtained as:

$$\dot{U}_{dc} = \frac{I_{dc}}{C_{dc}} - \frac{3}{2}\frac{v_{gd}i_{gd}}{C_{dc}U_{dc}}. \tag{17}$$

3.1.3. Inverter and Controller

The PV controller consisted of a voltage controller and a current controller, which can achieve main functions [22]. The voltage controller regulated the DC voltage to control or maximize the power extracted from the PV array. The current controller realized the control of an actual current to the current reference value. Figure 5 shows the structures of voltage and current controllers. i^*_{gq} was assigned as 0. The voltage and current control equations were given as Equations (18) and (19), respectively:

$$\begin{cases} i^*_{gd} = K_{pv}(U^*_{dc} - U_{dc}) + K_{iv}\int (U^*_{dc} - U_{dc})dt \\ i^*_{gq} = 0 \end{cases}, \tag{18}$$

$$\begin{cases} v^*_{kd} = K_{pi}(i^*_{gd} - i_{gd}) + K_{ii}\int (i^*_{gd} - i_{gd})dt - wL_f i_{gq} + v_{gd} \\ v^*_{kq} = K_{pi}(i^*_{gq} - i_{gq}) + K_{ii}\int (i^*_{gq} - i_{gq})dt + wL_f i_{gd} + v_{gq} \end{cases}. \tag{19}$$

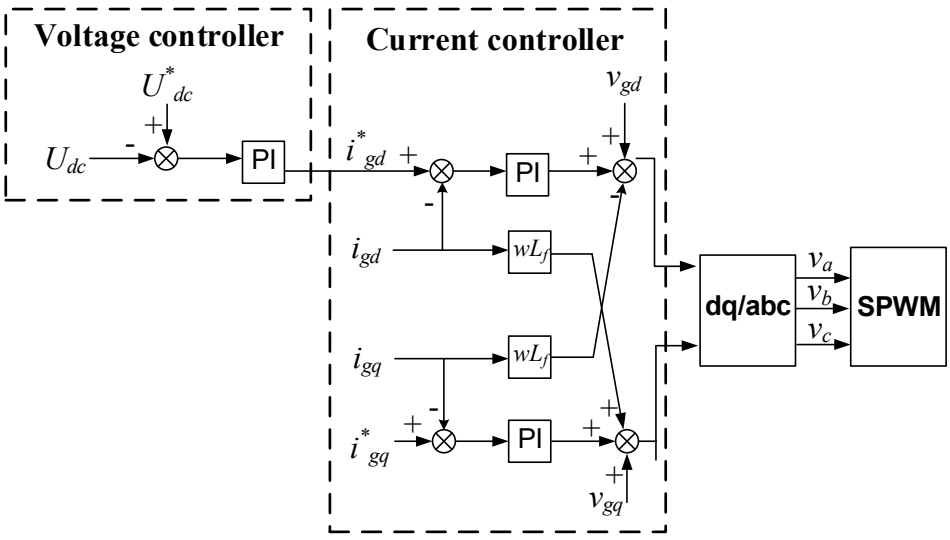


Figure 5. The structure of controllers. Symbols: U^*_{dc}, the reference value of a DC-side voltage; i^*_{gd}, the reference value of a *d*-axis current; i^*_{gq}, the reference value of a *q*-axis current; i_{gd}, the *d*-axis current; i_{gq}, the *q*-axis current; v_{gd}, the *d*-axis voltage; v_{gq}, the *q*-axis voltage; ω, the angular frequency of the system.

X_v, Y_d, and Y_q were introduced as the state variables of the controllers [23]. The dynamic equations were described as:

$$\begin{aligned} \dot{X}_v &= U_{dc}^* - U_{dc}, \\ \dot{Y}_d &= i_{gd}^* - i_{gd}, \\ \dot{Y}_q &= i_{gq}^* - i_{gq} \end{aligned} \tag{20}$$

Considering the structure of the filter L_f, the dynamic equations of filterwere written as:

$$\begin{cases} L_f \dot{i}_{gd} = v_{kd} - v_{gd} + wL_f i_{gq} \\ L_f \dot{i}_{gq} = v_{kq} - v_{gq} - wL_f i_{gd} \end{cases}. \tag{21}$$

3.1.4. PV Generation

According to Equations (14), (17), (20), and (21), a small-signal model of a PV generation model can be obtained by linearization as following:

$$\Delta \dot{X}_{PV} = A_{PV} \Delta X_{PV} + B_{PV} \Delta V_{gdq}, \tag{22}$$

where $\Delta X_{PV} = [\Delta U_{dc}, \Delta X_V, \Delta Y_d, \Delta Y_q, \Delta i_{gd}, \Delta i_{gq}]^{\mathrm{T}}$, and the coefficient matrices are shown in Equations (23) and (24):

$$A_{PV} = \begin{bmatrix} \frac{3v_{gd}i_{gd}}{2C_{dc}U_{dc}^2} - \frac{mI_{sc}[1-C_1(e^{\frac{U_{dc}}{nC_2U_{oc}}}-1)]}{C_{dc}U_{dc}} & 0 & 0 & 0 & -\frac{3v_{gd}}{2C_{dc}U_{dc}} & 0 \\ 1 & 0 & 0 & 0 & 0 & 0 \\ K_{pv} & K_{iv} & 0 & 0 & -1 & 0 \\ 0 & 0 & 0 & 0 & 0 & -1 \\ \frac{K_{pi}K_{pv}}{L_f} & \frac{K_{iv}K_{pi}}{L_f} & \frac{K_{ii}}{L_f} & 0 & -\frac{K_{pi}}{L_f} & 0 \\ 0 & 0 & 0 & \frac{K_{ii}}{L_f} & 0 & -\frac{K_{pi}}{L_f} \end{bmatrix}, \tag{23}$$

$$B_{PV} = \begin{bmatrix} -\frac{3i_{gd}}{2C_{dc}U_{dc}} & 0 & 0 & 0 & 0 & 0 \\ 0 & 0 & 0 & 0 & 0 & 0 \end{bmatrix}^{\mathrm{T}}. \tag{24}$$

3.2. Hydropower Unit

3.2.1. Synchronous Generator

All generators were synchronous generators with a fourth-order model. The model was shown as:

$$\begin{aligned} \dot{\delta} &= \omega_0(\omega - 1), \\ 2H\dot{\omega} &= (P_m - P_e - D(1-\omega)), \\ \dot{E}_q' &= (-E_q' - (X_d - X_d')I_d + E_{fd})/T_{d0}', \\ \dot{E}_d &= (-E_q' + (X_q - X_q')I_q)/T_{q0}' \end{aligned} \tag{25}$$

where ω_0 is the base angular frequency, H is the inertia constant, P_m is the mechanical power, P_e is the electromagnetic power, D is the damping coefficient, E'_d and E'_q are the d-axis and q-axis transient voltages, respectively, X_d and X_q are the unsaturated reactances, X'_d and X'_q are the unsaturated transient reactances, I_d and I_q are the d-axis and q-axis currents, respectively, E_{fd} is the excitation voltage, and T'_{d0} and T'_{q0} are the unsaturated subtransient times. The detailed meanings of the symbols is given in [19].

3.2.2. Exciter

An excitation system is the main cause of low-frequency oscillations, and it is unclear whether it has an effect on ultralow-frequency oscillations. Therefore, a detailed typical fourth-order excitation system was selected [24]. The block diagram of the excitation system is shown in Figure 6.

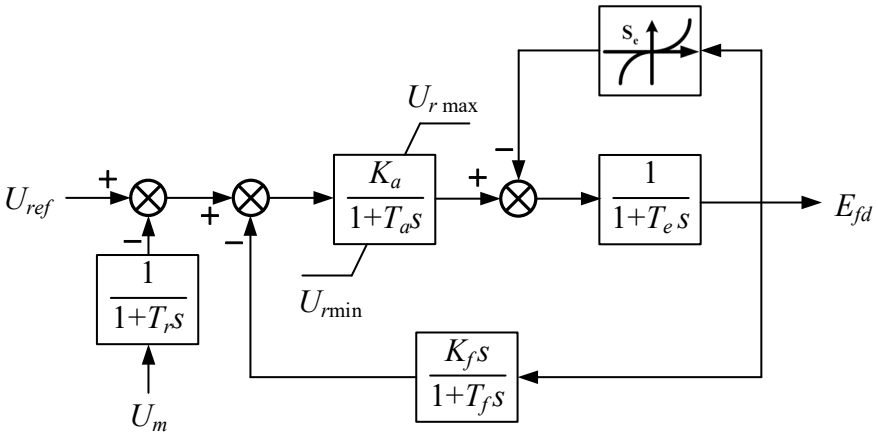


Figure 6. Block diagram of the exciter.

U_{ex1}, U_{ex2}, and U_{ex3} were selected as the state variables. The mathematical model was shown as:

$$\begin{aligned} \dot{U}_{ex1} &= (U_m - U_{ex1})/T_r, \\ \dot{U}_{ex2} &= (K_a(U_{ref} - U_{ex1} - U_{ex2} - K_f E_{fd}/T_f) - U_{ex2})/T_a, \\ \dot{U}_{ex3} &= -(K_f E_{fd}/T_f + U_{ex3}), \\ \dot{E}_{fd} &= -(E_{fd}(1 + S_e) - U_{ex})/T_e \end{aligned} \tag{26}$$

where U_m, U_{ref}, and E_{fd} are the terminal voltage, reference input excitation voltage, and generator excitation potential, respectively, and K_a, K_f, T_a, T_f, T_r, and T_e are the amplifier gain, stabilizer gain, amplifier time constant, stabilizer time constant, measurement time constant, and excitation circuit time constant, respectively. The expressions of S_e and U_{ex} were shown as:

$$S_e = A_e\left(e^{B_e|E_{fd}|} - 1\right), \tag{27}$$

$$\begin{aligned} U_{ex} = \; & \frac{1}{2}U_{ex2}(\mathrm{sgn}((U_{r\max} - U_{ex2})(U_{ex2} - U_{r\min})) + 1) + \frac{1}{2}U_{r\max}(\mathrm{sgn}(U_{ex2} - U_{r\max}) + 1) \\ & + \frac{1}{2}U_{r\min}(\mathrm{sgn}(U_{r\min} - U_{ex2}) + 1) \end{aligned} \tag{28}$$

3.2.3. Governor and Turbine

In order to study ultralow-frequency oscillation, a detailed model of a governor and a turbine was selected [19]. It consisted of a regulating system, an electro-hydraulic servo system, and a turbine model. In an actual running system, K_D is generally set to 0. The hydraulic turbine and the PID governor are shown in Figure 7.

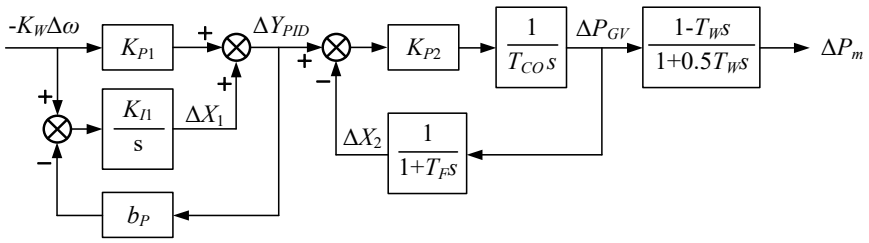


Figure 7. Block diagram of a water turbine and a PID governor. Symbols: K_W, the gain of frequency deviation; b_p, permanent difference coefficient; K_{P1}, the gain of the governor; K_{I1}, the integral gain of the governor; K_{P2}, the gain of the servo system; T_F, the time constant of stroke feedback; T_W, the time constant of the water hammer.

X_1, X_2, P_{GV}, and P_m were seleted as the state variables of the model composed of a governor and a turbine.

3.3. Small-Signal Model of the Integrated PV-Hydro System

Suppose the system has n generator nodes, one PV generation, and l connected nodes. The lines and loads of the system can be expressed by algebraic Equation (29):

$$\begin{bmatrix} \Delta I_{dq1} \\ \cdots \\ \Delta I_{dq(n+1)} \\ 0 \\ \cdots \\ 0 \end{bmatrix} = \begin{bmatrix} Y_{11} & Y_{12} \\ Y_{21} & Y_{22} \end{bmatrix} \begin{bmatrix} \Delta V_{dq1} \\ \cdots \\ \Delta V_{dq(n+1)} \\ \Delta V_{dq(n+2)} \\ \cdots \\ \Delta V_{dq(n+l+1)} \end{bmatrix}. \tag{29}$$

By eliminating the connected nodes, the nodal admittance matrix can be simplified as:

$$\begin{bmatrix} \Delta I_{dq1} \\ \cdots \\ \Delta I_{dq(n+1)} \end{bmatrix} = (Y_{11} - Y_{12}Y_{22}^{-1}Y_{21}) \begin{bmatrix} \Delta V_{dq1} \\ \cdots \\ \Delta V_{dq(n+1)} \end{bmatrix}. \tag{30}$$

By integrating the PV small-signal model into the hydropower system, a small-signal dynamic model of the integrated system can be obtained as:

$$\begin{bmatrix} \dot{\Delta x}_{w1} \\ \cdots \\ \dot{\Delta x}_{wn} \\ \dot{\Delta x}_{PV} \end{bmatrix} = A_{sys} \begin{bmatrix} \Delta x_{w1} \\ \cdots \\ \Delta x_{wn} \\ \Delta x_{PV} \end{bmatrix}, \tag{31}$$

where $\Delta X_{sys} = [\Delta X_{w1}, \ldots, \Delta X_{wn}, \Delta X_{PV}]^{\mathrm{T}}$, A_{sys} is the complete system state matrix, and $\Delta X_{w1}, \ldots, \Delta X_{wn}$ are the state variables of n hydropower units, and ΔX_{PV} is the state variables of the PV generation. By analyzing the eigenvalues and the eigenstructures of A_{sys}, the system small-signal stability can be evaluated.

4. Small-Signal Stability Analysis

According to the small-signal model above, the effect of grid-connected PV generation on ultralow-frequency oscillation was studied based on two test systems, i.e., a modified two-zone and four-machine system and an actual system.

- The two-zone and four-machine system is a typical benchmark system with standard parameters to study power system oscillations [19]. This paper selected it as a case study system and added PV generation into this system. The steam turbines of the two-zone and four-machine system were replaced by water turbines for hydropower studies.
- In order to study the effect of PV generation in an actual system, an actual integrated PV-hydro system in Sichuan Province, China was selected, so that the research has practical significance.

4.1. Modified Two-Area and Four-Machine System

Based on the two-zone and four-machine system, an integrated PV-hydro system was constructed. The structure of the integrated PV-hydro system is shown in Figure 8. The parameters of the two-zone and four-machine system can be found in Reference [19]. The characteristic matrix of the system can be obtained by Equation (31).

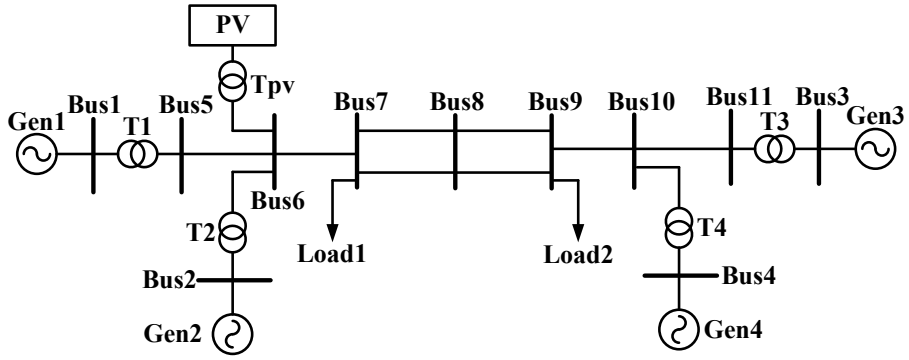


Figure 8. The structure of an integrated PV-hydro system. Gen1, Gen2, Gen3 and Gen4 are the abbreviations for the names of hydropower stations.

In order to make the damping characteristics of each hydropower unit different, different water hammer time constants were set for each hydroelectric unit. The detailed parameters of governors and turbines are shown in Table 1.

Table 1. The parameters of governors and turbines.

	Gen1	Gen2	Gen3	Gen4
T_w/s	1	1	3	3
K_P	2.6	2.6	2.6	2.6
K_I	6	6	6	6
K_D	0	0	0	0

The ultralow-frequency oscillation of the system calculated by the small-signal model is shown in Table 2. The oscillation frequency was less than 0.1 Hz, which belongs to the ultralow-frequency range.

Table 2. The ultralow-frequency oscillation.

Eigenvalues	Damping Ratio (%)	Frequency (Hz)
−0.0127 ± 0.1635i	7.73	0.026

4.1.1. Participation Factor Analysis

Participation factors are the multiplication of the corresponding elements in the right and left eigenvectors of a state matrix. It can be used for evaluating the association degree between state variables and modes. In this paper, we performed the participation factor analysis based on the state matrix A_{sys} in Equation (31).

The participation factors of state variables for the ultralow-frequency oscillation mode are shown in Figure 9. As can be seen from Figure 9, the dynamics of synchronous machines, governors, and turbines were mainly involved in the ultralow-frequency oscillation mode, and the generators with a larger T_w were more involved. The dynamics of PV hardly participate in the ultralow-frequency oscillation mode. This is mainly because PV generation uses power control modes and does not participate in the frequency regulation.

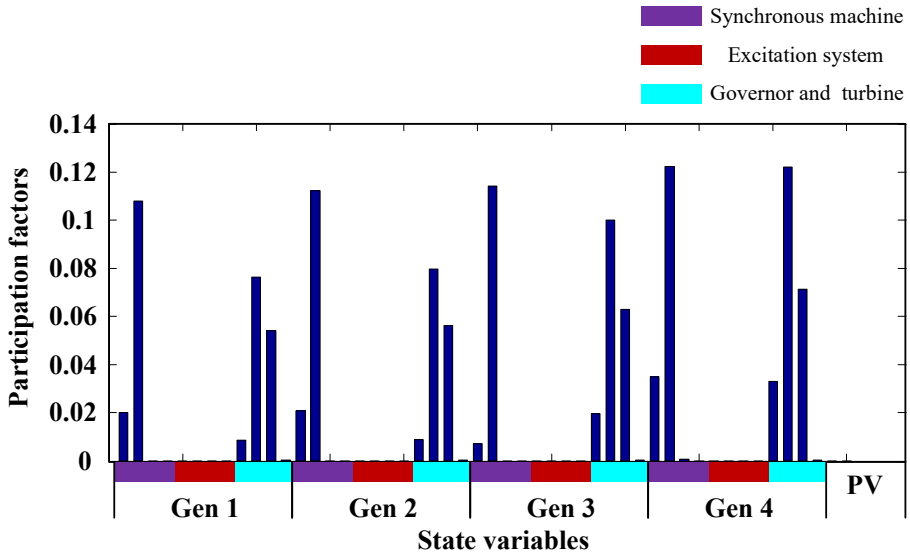


Figure 9. Participation factors. The state variables of synchronous machines contain δ, ω, E'_d, and E'_q. The state variables of excitation systems contain U_{ex1}, U_{ex2}, and U_{ex3}. The state variables of governors and turbines contain X_1, X_2, P_{GV}, and P_m. The state variables of PV generation contain U_{dc}, X_V, Y_d, Y_q, i_{gd}, and i_{gq}.

4.1.2. Different Output Powers

When the output power of PV generation increased from 100 to 600 MW, the root locus of the ultralow-frequency oscillation mode changed, as shown in Figure 10, and the corresponding damping ratio and frequency are shown in Table 3. In Figure 10, the abscissa axis correspond to the real parts of eigenvalues, and the vertical axis corresponds to the imaginary parts of eigenvalues. It can be seen from the results that the changes in PV output power had little effect on the ultralow-frequency oscillation mode.

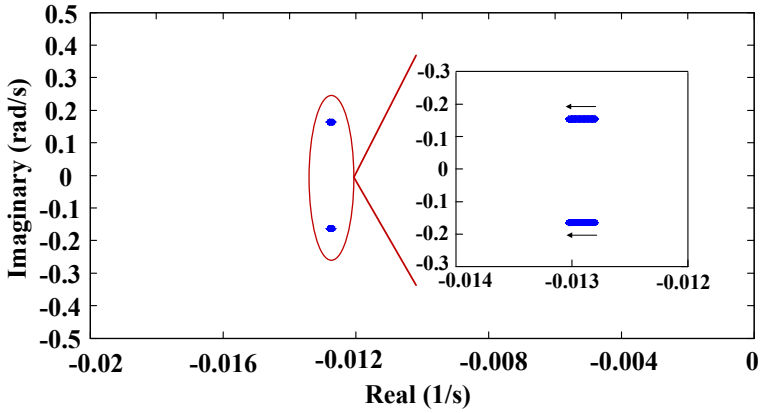


Figure 10. Root locus of the ultralow-frequency oscillation.

Table 3. Damping ratio and frequency with increasing of PV output power.

Output Power (MW)	Damping Ratio (%)	Frequency (Hz)
100	7.73	0.026
200	7.75	0.026
300	7.77	0.026
400	7.79	0.026
500	7.81	0.026
600	7.82	0.026

4.1.3. Different Locations

The ultralow-frequency oscillation modes for PV generation connected to different locations are shown in Table 4. It can be seen that the connections of PV generation with different buses had little effect on the ultralow-frequency oscillation mode.

Table 4. The ultralow-frequency oscillation modes for PV generation connected to different locations.

Location	Eigenvalues	Damping Ratio (%)	Frequency (Hz)
Bus 5	−0.0126 ± 0.1635i	7.71	0.026
Bus 6	−0.0127 ± 0.1635i	7.73	0.026
Bus 10	−0.0131 ± 0.1636i	7.96	0.026
Bus 11	−0.0131 ± 0.1636i	7.97	0.026

4.1.4. Replacing Generator

Table 5 shows the ultralow-frequency oscillation modes when a hydropower unit was replaced by PV generation. According to the results of the damping torque analysis, a larger T_w of a hydropower unit provided more negative damping. Because T_w values of Gen1 and Gen2 were small, they provided less negative damping to the system. When they were replaced by PV generation, the system damping ratio reduced. Since the T_w of Gens 3 and 4 were large, they provided more negative damping to the system. When they were replaced by PV generation, the system damping ratio was improved.

Table 5. The ultralow-frequency oscillation modes by replacing a generator.

Generator Replaced	Eigenvalues	Damping Ratio (%)	Frequency (Hz)
Gen 1	−0.0050 ± 0.1580i	3.14	0.025
Gen 2	−0.0049 ± 0.1580i	3.12	0.025
Gen 3	−0.0160 ± 0.1644i	9.64	0.026
Gen 4	−0.0159 ± 0.1644i	9.62	0.026

4.2. Actual System of a County in Sichuan Province, China

An integrated PV-hydro system in a county of Sichuan Province in China was selected as the second test system with its structure shown in Figure 11. The system was connected to an external grid through a double feeder, which could be disconnected from an outside grid and then achieve an islanded operation.

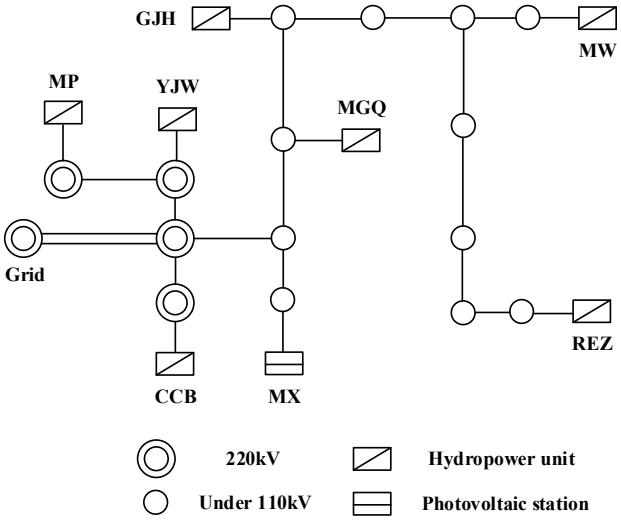


Figure 11. Structure diagram of a county town in China. MP, YJW, CCB, MGQ, GJH, MW, and REZ are the abbreviations for the names of hydropower stations, MX is the abbreviation for the name of a PV station.

The output powers of the sources are shown in Table 6. The ultralow-frequency oscillation modes of the system under different operating modes are shown in Table 7. When connected to the network, the overall damping of the system was relatively strong, since the external power grid can help stabilize the frequency. During island operation, the damping of the ultralow-frequency oscillation mode became smaller, and it was easier to excite the ultralow-frequency oscillation.

Table 6. The output powers of sources.

Name	Output Power (MW)	
	Grid-Connected Mode	Island Mode
MP	45	10
YJW	60	13
CCB	54	12
MHQ	36	12
GJH	44	10
MW	23	5
REZ	37	9
MX	100	20

Table 7. Ultralow-frequency oscillations under different operating modes.

Operating Mode	Eigenvalues	Damping Ratio (%)	Frequency (Hz)
On-grid	−1.172 ± 0.42i	94.2	0.066
Off-grid	−0.032 ± 0.33i	9.7	0.053

The participation factors are shown in Figure 12. Figure 12 indicates that the dynamics of PV hardly participated in the ultralow-frequency oscillation mode. The root locus of the PV output power increasing from 20 to 70 MW is shown in Figure 13. In Figure 13, the abscissa axis corresponds to the real parts of eigenvalues, and the vertical axis corresponds to the imaginary parts of eigenvalues. Figure 13 indicates that the root positions of the ultralow-frequency oscillation mode changed very little. The conclusion is the same as that obtained by studying the two-zone and four-machine system.

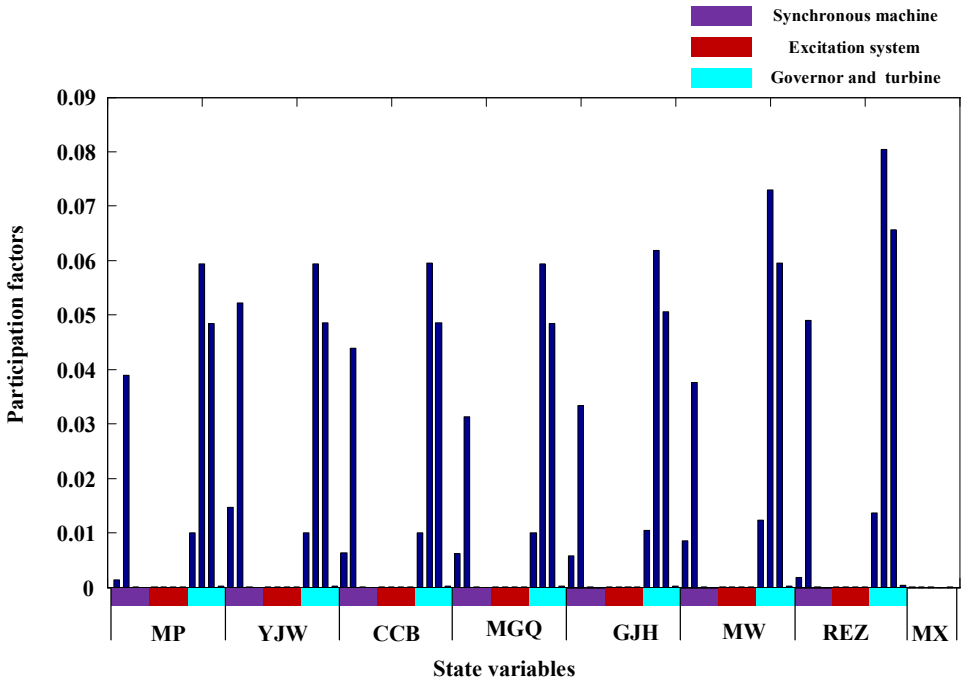


Figure 12. Participation factors. The state variables are the same as in Figure 9.

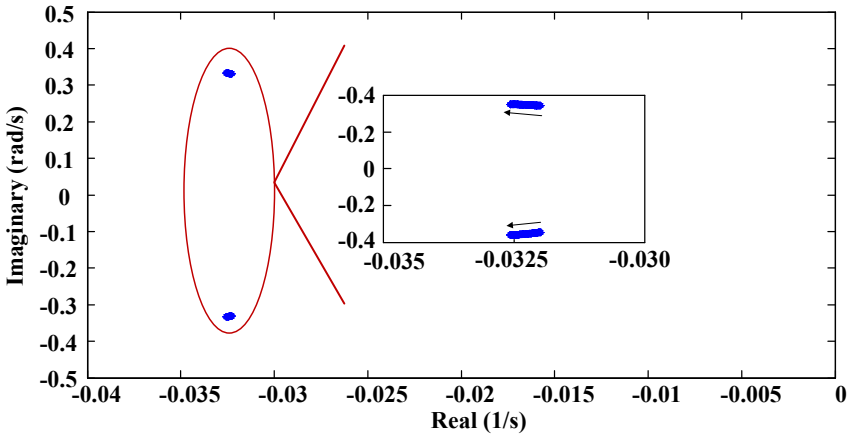


Figure 13. Root locus of the ultralow-frequency oscillation.

Remark: In order to diminish the negative influences of the ultralow-frequency oscillation, some methods have been proposed. First, by quitting the frequency regulation function of hydropwer generators with negative damping, the oscillation could be eliminated [25]. Second, some optimization methods for the PID parameters of hydropower governors were proposed, which take into account the tradeoff between the performance of primary frequency regulation and the suppression of ultralow-frequency oscillations [4]. In addition, some researchers have added a governor's power system stabilizer on the speed control side of a hydropower generator to increase its damping in the ultralow-frequency band, thereby suppressing ultralow-frequency oscillations [9]. In this paper, we mainly focused on analyzing the impact of PV generation on ultralow-frequency oscillations. The methods to suppress ultralow-frequency oscillations will be included in our future work.

5. Conclusions

In this paper, a small-signal dynamic model of an integrated PV-hydro system was established. The small-signal stability analysis method was used to analyze and study the impact of PV generation on ultralow-frequency oscillation modes. The main conclusions are summarized as follows:

(1) The dynamics of synchronizers, governors, and turbines were mainly involved in ultralow-frequency oscillation modes, while the dynamics of PV were hardly involved.

(2) Different output powers and locations of PV generation changed the distribution of the power flow but had very little effect on ultralow-frequency oscillation modes.

(3) When a synchronous machine in the system was replaced by PV generation, the ultralow-frequency oscillation mode changed significantly. In addition, when the negative damping characteristic of the replaced unit was relatively strong, the damping of the system was improved after the replacement.

Ultralow-frequency oscillation is a special phenomenon of hydropower systems. It is mainly caused by the negative damping of governors and turbines in the ultralow-frequency band. However, PV generation usually use power control modes and do not reserve power for frequency regulation. The reason for the ultralow-frequency oscillations of hydropower systems is mainly the small-signal stability problem due to frequency regulation. With the power control mode, the PV generation did not participate in frequency regulation, and thus it has little influence on ultralow-frequency oscillation. Our future research will focus on the influence of PV generation on ultralow-frequency oscillation when it is involved in the system frequency regulation.

Author Contributions: S.W. and X.W. did modeling and analysis. G.C. provided the test system data. S.W. and X.W. wrote the manuscript. Y.X. revised the manuscript. All the authors have read and approved the final manuscript. All authors have read and agreed to the published version of the manuscript.

Funding: This research was supported in part by the National Key R&D Program of China (2018YFB0905200), in part by the National Natural Science Foundation of China (51807005).

Conflicts of Interest: The authors declare no conflicts of interest.

Nomenclature

T_w	water hammer time constant of a turbine
K_P	proportional parameter of a governor
K_I	integral parameter of a governor
K_D	differential parameter of a governor
D_T	damping torque
S_T	synchronous torque
C_{dc}	DC capacitor
U_{dc}	DC-side output voltage
V_k	AC-side output voltage
L_f	AC inductor
i_g	AC-side output current
V_g	voltage of a parallel point with a power system
I_{sc}	short-circuit current of PV cells
U_{oc}	open-circuit voltage of PV cells
I_m	current of PV cells at the maximum power
U_m	voltage of PV cells at the maximum power
T	temperature of PV cells
T_{air}	temperature of the air
S	light intensity
U_{ocref}	open-circuit voltage in standard conditions
I_{scref}	short-circuit current in standard conditions
U_{mref}	voltage of the maximum power point in standard conditions
S_{ref}	light intensity in standard conditions
T_{ref}	temperature in standard conditions

k	compensation coefficient
α	compensation coefficient
β	compensation coefficient
γ	compensation coefficient
U^*_{dc}	reference value of a DC-side voltage
i^*_{gd}	reference value of a d-axis current
i^*_{gq}	reference value of a q-axis current
i_{gd}	d-axis current
i_{gq}	q-axis current
v_{gd}	d-axis voltage
v_{gq}	q-axis voltage
ω	angular frequency of a system
ω_0	base angular frequency
H	inertia constant of a synchronous machine
P_m	mechanical power
P_e	electromagnetic power
D	damping coefficient of a synchronous machine
E'_d	d-axis transient voltage
E'_q	q-axis transient voltage
X_d	d-axis unsaturated reactance
X_q	q-axis unsaturated reactance
X'_d	d-axis unsaturated transient reactance
X'_q	q-axis unsaturated transient reactance
I_d	d-axis current
I_q	q-axis current
E_{fd}	excitation voltage
T'_{d0}	d-axis unsaturated subtransient time
T'_{q0}	q-axis unsaturated subtransient time
U_m	terminal voltage
U_{ref}	reference input excitation voltage
K_a	amplifier gain
K_f	stabilizer gain
T_a	time constant of an amplifer
T_f	time constant of a stabilizer
T_r	time constant of a measurement
K_W	gain of a frequency deviation
b_p	permanent difference coefficient
K_{P1}	gain of a governor
K_{I1}	integral gain of a governor
K_{P2}	gain of a servo system
T_F	time constant of stroke feedback
T_W	time constant of water hammer

References

1. Schleif, F.R.; White, J.H. Damping for the Northwest-Southwest Tieline Oscillations—An Analog Study. *IEEE Trans. Power Appar. Syst.* **1966**, *PAS-85*, 1239–1247. [CrossRef]
2. Villegas, H.N. Electromechanical oscillations in hydro dominant power systems: An application to the Colombian power system. Master's Thesis, Iowa State University, Ames, IA, USA, 2011.
3. Fu, C.; Liu, Y.; Tu, L.; Li, P.; Hong, C.; Li, P.; Wu, C.; Xu, M.; Zhao, R. Experiment and Analysis on Asynchronously Interconnected System of Yunnan Power Grid and Main Grid of China Southern Power Grid. *South. Power Syst. Technol.* **2016**, *10*, 1–5.
4. Chen, G.; Tang, F.; Shi, H.; Yu, R.; Wang, G.; Ding, L.; Liu, B.; Lu, X. Optimization Strategy of Hydrogovernors for Eliminating Ultralow-Frequency Oscillations in Hydrodominant Power Systems. *IEEE J. Emerg. Sel. Top. Power Electron.* **2018**, *6*, 1086–1094. [CrossRef]

5. Lu, X.; Chen, L.; Chen, Y.; Min, Y.; Hou, J.; Liu, Y. Ultra-low-frequency Oscillation of Power System Primary Frequency Regulation. *Autom. Electr. Power Syst.* **2017**, *41*, 64–70.
6. Zheng, C.; Ding, G.; Liu, B.; Zhang, X.; Wang, J.; Xue, A.; Bi, T. Analysis and control to the ultra-low frequency oscillation in southwest power grid of China: A case study. In Proceedings of the 2018 Chinese Control And Decision Conference, Shenyang, China, 9–11 June 2018; pp. 5721–5724.
7. Deng, W.; Wang, D.; Wei, M.; Zhou, X.; Wu, S.; He, P.; Kang, J. Influencing Mechanism Study on Turbine Governor Parameters Upon Ultra-low Frequency Oscillation of Power System. *Power Syst. Technol.* **2019**, *43*, 1371–1377.
8. Huang, W.; Duan, R.; Jiang, C.; Zhou, J.; Gan, D. Stability Analysis of Ultra-low Frequency Oscillation and Governor Parameter Optimization for Multi-machine System. *Autom. Electr. Power Syst.* **2018**, *42*, 185–193.
9. Liu, S.; Wang, D.; Ma, N.; Deng, W.; Zhou, X.; Wu, S.; He, P. Study on Characteristics and Suppressing Countermeasures of Ultra-low Frequency Oscillation Caused by Hydropower Units. *Proc. CSEE* **2019**, *39*, 5354–5362.
10. Rashid, K.; Ellingwood, K.; Safdarnejad, S.M.; Powell, K.M. Designing Flexibility into a Hybrid Solar Thermal Power Plant by Real-Time, Adaptive Heat Integration. *Comput. Aided Chem. Eng.* **2019**, *47*, 457–462.
11. Jong, P.D.; Barreto, T.B.; Tanajura, C.A.S.; Kouloukoui, D.; Oliveira-Esquerre, K.P.; Kiperstok, A.; Torres, E.A. Estimating the impact of climate change on wind and solar energy in Brazil using a South American regional climate model. *Renew. Energy* **2019**, *141*, 390–401. [CrossRef]
12. Shah, R.; Mithulananthan, N.; Bansal, R.C. Oscillatory stability analysis with high penetrations of large-scale photovoltaic generation. *Energy Convers. Manag.* **2013**, *65*, 420–429. [CrossRef]
13. Ding, M.; Wang, W.; Wang, X.; Song, Y.; Chen, D.; Sun, M. A Review on the Effect of Large-scale PV Generation on Power Systems. *Proc. CSEE* **2014**, *34*, 1–14.
14. Quintero, J.; Vittal, V.; Heydt, G.T.; Zhang, H. The Impact of Increased Penetration of Converter Control-Based Generators on Power System Modes of Oscillation. *IEEE Trans. Power Syst.* **2014**, *29*, 2248–2256. [CrossRef]
15. Du, W.; Wang, H.; Xiao, L. Power system small-signal stability as affected by grid-connected photovoltaic generation. *Eur. Trans. Electr. Power* **2012**, *22*, 688–703. [CrossRef]
16. Eftekharnejad, S.; Vittal, V.; Heydt, G.T.; Keel, B.; Loehr, J. Impact of increased penetration of photovoltaic generation on power systems. *IEEE Trans. Power Syst.* **2013**, *28*, 893–901. [CrossRef]
17. Eftekharnejad, S.; Vittal, V.; Heydt, G.T.; Keel, B.; Loehr, J.S. Small Signal Stability Assessment of Power Systems with Increased Penetration of Photovoltaic Generation: A Case Study. *IEEE Trans. Sustain. Energy* **2013**, *4*, 960–967. [CrossRef]
18. Ge, J.; Du, H.; Zhao, D.; Ma, J.; Qian, M.; Zhu, L. Influences of Grid-connected Photovoltaic Power Plants on Low Frequency Oscillation of Multi-machine Power Systems. *Autom. Electr. Power Syst.* **2016**, *40*, 63–70.
19. Kundur, P.; Balu, N.J.; Lauby, M.G. *Power System Stability and Control*; McGraw-Hill: New York, NY, USA, 1994.
20. Rashid, K.; Mohammadi, K.; Powell, K. Dynamic simulation and techno-economic analysis of a concentrated solar power (CSP) plant hybridized with both thermal energy storage and natural gas. *J. Clean. Prod.* **2020**, *248*, 119193. [CrossRef]
21. Deng, J.; Xia, N.; Yin, J.; Jin, J.; Peng, S.; Wang, T. Small-Signal Modeling and Parameter Optimization Design for Photovoltaic Virtual Synchronous Generator. *Energies* **2020**, *13*, 398. [CrossRef]
22. Yazdani, A.; Dash, P.P. A Control Methodology and Characterization of Dynamics for a Photovoltaic (PV) System Interfaced With a Distribution Network. *IEEE Trans. Power Deliv.* **2009**, *24*, 1538–1551. [CrossRef]
23. Pogaku, N.; Prodanovic, M.; Green, T.C. Modeling, Analysis and Testing of Autonomous Operation of an Inverter-Based Microgrid. *IEEE Trans. Power Electron.* **2007**, *22*, 613–625. [CrossRef]
24. Shi, J.; Shen, C. Impact of DFIG wind power on power system small signal stability. In Proceedings of the 2013 IEEE Pes Innov. Smart Grid Technol. Conference, Washington, DC, USA, 24–27 February 2013; pp. 1–6.
25. Chen, L.; Lu, X.; Chen, Y.; Min, Y.; Mo, K.; Liu, Y. Online Analysis and Emergency Control of Ultra-low-frequency Oscillations Using Transient Energy Flow. *Autom. Electr. Power Syst.* **2017**, *41*, 9–14.



© 2020 by the authors. Licensee MDPI, Basel, Switzerland. This article is an open access article distributed under the terms and conditions of the Creative Commons Attribution (CC BY) license (http://creativecommons.org/licenses/by/4.0/).